ADVANCED ENERGY & SUSTAINABILITY RESEARCH
Open Access
www.advenergysustres.com

Dualism of Remarkable Magnesium Ion Conduction with Low Activation Energy over a Wide Temperature Range versus Limited Stability of the Hybrid Composite Electrolyte Mg-MOF-74/MgX_2/Propylene Carbonate

Ruben Maile, Zhixuan Wei, Andreas Johannes Achazi, Kangli Wang, Pascal Henkel, Doreen Mollenhauer, Jürgen Janek,* and Klaus Müller-Buschbaum**

A metal–organic framework (MOF) quasi-solid-state Mg^{2+}-ion conductor is prepared with a conductivity of 0.6×10^{-4} S cm^{-1} already at room temperature. Mg-MOF-74 acts as host for MgX_2 ($X = Cl^-$, Br^-, BF_4^-) dissolved in propylene carbonate, leading to dry free-flowing powders with liquid electrolyte exhibiting low activation energy of 0.2 eV with Arrhenius-type behavior (233–333 K). Different halides and pseudohalides reveal an influence of the anions on ionic conductivity, activation energy, and chemical stability. High transference numbers 0.45–0.80 for Mg^{2+} ions are recorded, being among the highest reported with small and low-cost halides. Against magnesium, an insulating solid electrolyte interface layer forms that prevents a steady-state and full-MOF decomposition, as shown by powder X-ray diffraction, FTIR, and Raman spectroscopy. Comparison with pure propylene carbonate shows that the electrolyte is enhanced by MOF addition. Computational studies using density functional theory (DFT) calculations of complexes in solution indicate correlations between the activation energy for Mg^{2+} migration through the MOF and the Gibbs energy needed to form charged Mg compounds in solution. Furthermore, DFT calculations of complexes within the MOF pore reveal variations in binding energy and charge transfer correlating with experimental transference numbers. Altogether, the high potential of MOFs for quasi-solid-state electrolytes with multivalent cations stability issues are illuminated.

1. Introduction

The ever-growing demand for high-performance batteries with high volumetric and gravimetric energy densities for applications in electric vehicles or consumer electronics leads to market expectations for lithium-ion batteries in the TWh range of energy capacity. This raises questions concerning the supply with raw materials and processed compounds,[1] and drives extensive research for alternative electrolyte concepts relying, e.g., on Na^+ or Mg^{2+} ions. Their higher abundance and lower cost compared to lithium, together with the large number of their solid-state compounds, can help to release economic pressure in the lithium battery market. While sodium ion batteries are already close to commercialization, magnesium-based batteries are still in an infant state. Magnesium attracts severe interest, due to its higher volumetric energy density compared to lithium [w_{vol} (Mg) = 3832 mAh cm^{-3} vs w_{vol} (Li) = 2061 mAh cm^{-3}]. However, the comparably poor kinetics of magnesium transport in condensed phases is an issue.

R. Maile, K. Müller-Buschbaum
Institute of Inorganic and Analytical Chemistry
Justus-Liebig-University Giessen
Heinrich-Buff-Ring 17, 35392 Giessen, Germany
E-mail: Klaus.Mueller-Buschbaum@anorg.chemie.uni-giessen.de

The ORCID identification number(s) for the author(s) of this article can be found under https://doi.org/10.1002/aesr.202300288.

[+]Present address: Department of Applied Physics, Aalto University, P.O. Box 11100, FI00076 Aalto, Finland

DOI: 10.1002/aesr.202300288

Z. Wei, A. J. Achazi, K. Wang, P. Henkel,[+] D. Mollenhauer, J. Janek
Institute of Physical Chemistry & Center for Materials Research
Justus-Liebig-University Giessen
Heinrich-Buff-Ring 17, 35392 Giessen, Germany
E-mail: doreen.mollenhauer@phys.chemie.uni-giessen.de; juergen.janek@pc.jlug.de

Z. Wei, A. J. Achazi, K. Wang, P. Henkel, D. Mollenhauer, J. Janek, K. Müller-Buschbaum
Center for Materials Research (LaMa)
Justus-Liebig-University Giessen
Heinrich-Buff-Ring 16, 35392 Giessen, Germany

The double-charged and small Mg^{2+} ion is highly polarizing the surrounding environment, and requires other electrolyte concepts.[2] Liquid electrolytes with sufficient conductivity and stability have been reported, such as $Mg[B(hfip)_4]_2$, a fluorinated alkoxyborate[3,4] or $Mg[B(O_2C_2(CF_3)_4)_2]_2$.[5] Solid electrolytes, which may also offer the perspective for solid-state cells or at least for solid-state separators or functional layers, with high ionic conductivity at room temperature have rarely been reported.[6]

Ionic conductivities higher than 1 mS cm^{-1} that would be necessary to compete with state-of-the-art lithium or sodium solid electrolytes have yet not been reported. Satisfying ionic conductivities were only reached at high temperatures in various Mg compounds.[7,8] Of all solid-state compounds, a room temperature conductivity of up to 10^{-4} S cm^{-1} was achieved to date only with the spinel-type phase $MgSc_2Se_4$, which is a mixed conductor that also has a non-negligible electronic conductivity.[9] Still, a solid, electronically insulating and well Mg^{2+} ion conducting material is missing and the diffusion of the divalent Mg ion with its strong Coulomb interaction with surrounding stiff lattices comes along with high activation energies. To circumvent this problem, metal–organic framework (MOF) materials have recently come into the focus of electrolyte research. As solid, but porous materials, they can be loaded with dissolved salts resulting in a quasi-solid-state electrolyte. The activation energy for Mg ion migration can be lowered significantly[10] and the contact of the electrolyte with anode and cathode can be improved.[11] Further advantages of solid electrolytes, such as higher thermal stability and higher safety, could also be obtained.[12] Furthermore, MOFs can also improve the performance of the incorporated electrolyte in terms of Mg^{2+} transference number by trapping of anions,[13,14] or enable conduction at lower temperatures by reducing the melting temperature of the incorporated electrolyte.[15] Therefore, research on MOF compounds as ionic conductors is rising during the last few years; however, yet mostly for Li-ion conductors.[16–18] Meanwhile, pioneering work on Mg^{2+} conduction in MOFs has also recently been published, showing the potential of this type of electrolyte.[19–21] For MIL-101 and MOF-74 loaded with $Mg(TFSI)_2$, ionic conductivities up to 1.9 S cm^{-1} and high transference numbers of Mg were achieved after vapor adsorption of organic molecules such as acetonitrile or methanol.[22,23] With UiO-66 loaded with $Mg(TFSI)_2$ and EMIM-TFSI as ionic liquid quasi-solid-state battery cell construction was possible, and stable cycling for 200 times was demonstrated without dendrite formation.[24] This is the basis for our interest in further advancing MOF-based electrolytes.

So far, there are two different types of liquid electrolytes used to achieve ionic conductivity in MOFs. The first one uses carbonates as solvent for inorganic salts,[25] while the second one substitutes carbonates with ionic liquids.[26] Each method has its own merits and problems.[18] Whereas ionic liquids have lower vapor pressure and are less flammable resulting in higher stability and safety,[27] they also exhibit high viscosities especially at lower temperatures.[28] Additionally, the electrolyte acts as a charge carrier itself, lowering the transference number,[29] i.e., the amount of charge which is transported by Li^+, Na^+, or Mg^{2+}. These disadvantages can potentially be overcome by the use of carbonates, which are already used in most battery applications and therefore suitable for direct usage. Nonetheless, the reported ionic conductivity and stability are usually lower.[30]

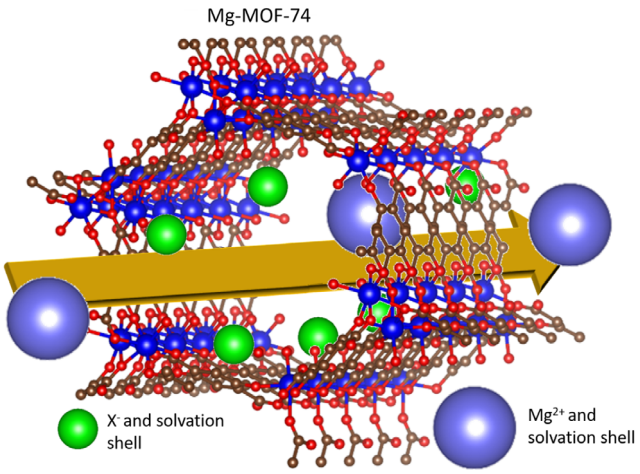

Figure 1. Scheme of Mg-MOF-74 with mobile Mg^{2+} ions moving into the direction of the anode and X^- ($X^- = Cl^-$, Br^-, BF_4^-). Only some Mg^{2+} and X^- and a representative of their solvation spheres are shown; the exact ratio of MgX_2 to MOF is not shown for clarity. Solvent molecules are not depicted for clarity.

As host material for liquid electrolytes, a MOF should preferably possess pore channels without narrowing between the pores to promote smooth conduction, as ion mobility is limited by the smallest radii. A system suitable for further development for industrial scale has preferably a well-scalable, cheap, and fast synthesis and is stable against water and air. Therefore, in the present report we used Mg-MOF-74 as host, propylene carbonate (PC) as liquid electrolyte with dissolved MgX_2 ($X = Cl^-$, Br^-, BF_4^-) as charge carrier (**Figure 1**). As key result, we present a well-conducting composite material Mg-MOF-74 0.4 MgX_2 3.8 PC ($X = Cl^-$, Br^-, BF_4^-), denoted in the following as MgX_2·PC@Mg-MOF-74, showing low activation energy, high ionic conductivity, and transference number of magnesium even at low temperatures. Computational calculations corroborate well with the experimental results. These highly promising data come along with low electrochemical stability, a possible downside of many MOFs.

2. Discussion

2.1. Structure and Morphology

As basis for the hybrid composite electrolyte, Mg-MOF-74 was synthesized, activated, impregnated, and characterized each after synthesis, activation, and impregnation. Also, all data shown belong to only one synthesized batch of the MOF to avoid synthesis-dependent differences in the material.

Powder X-ray diffraction (PXRD) patterns were recorded and compared to reference patterns,[31] as shown in **Figure 2**a. This indicates a highly crystalline powder of Mg-MOF-74 with the space group R-$\bar{3}$ and cell parameters of $a = b = 26.026$ Å and $c = 6.759$ Å with $\alpha = \beta = 90°$ and $\gamma = 120°$.[31] Reflection positions of the crystal structure remained the same after impregnation with different Mg salts (Figure 2b), with no additional reflections of Mg salts or other phases, but some minor reflection intensities

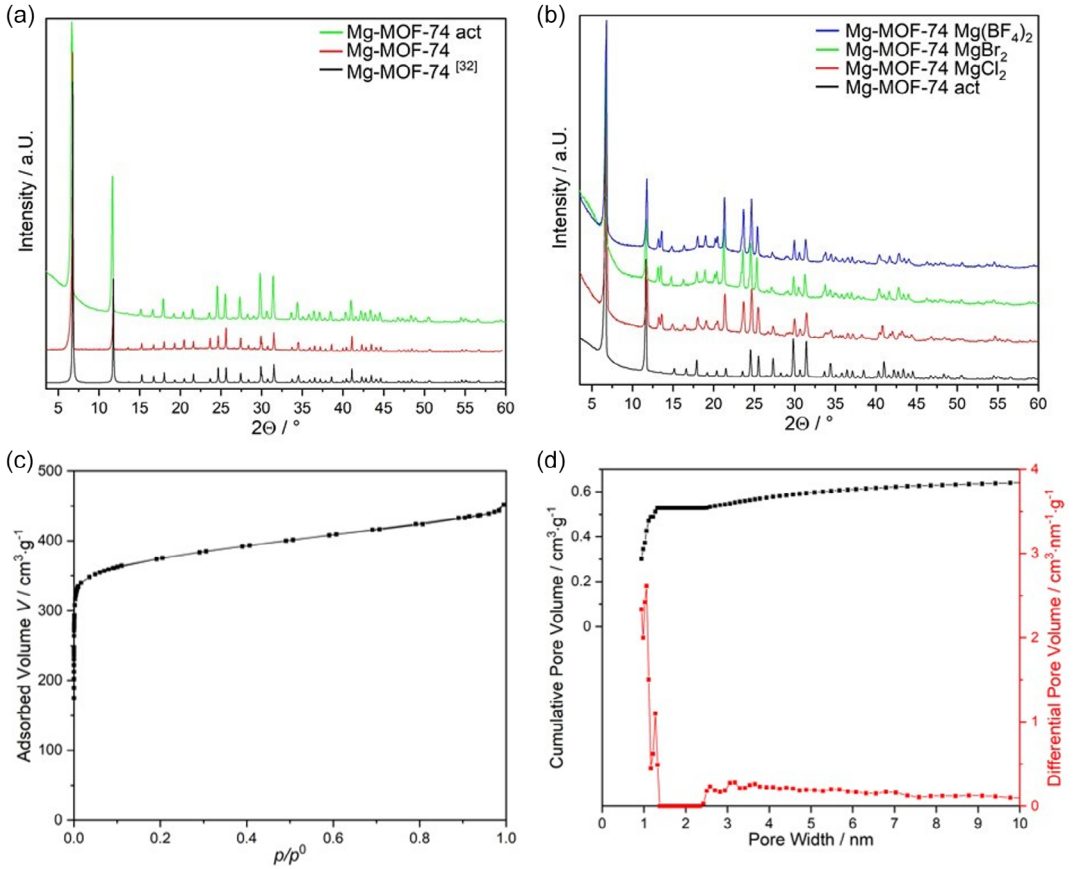

Figure 2. a) PXRD patterns of Mg-MOF-74 reference samples (literature, as-synthesized, and activated); b) PXRD of Mg-MOF-74 activated and loaded

of the activated MOF structure increase significantly upon impregnation. This indicates that the salts used for impregnation are mostly loaded into the pores, as a decoration of only the outer surface of the MOF particles would not lead to the observed changes in form factors but, e.g., additional reflections of side phases.[32]

In order to determine the degree of available inner surface, adsorption isotherms were recorded. The N_2-physisorption isotherm is depicted in Figure 2c and is described as Type 1(a) isotherm[33] generated by micropores. Brunauer–Emmett–Teller (BET) analysis reveals a large BET surface area of 1470 $m^2 g^{-1}$. This is close to the highest published value for Mg-MOF-74[34] and confirms activation of the MOF. The calculated pore size distribution suggests that most pores have a diameter of 12 Å, close to the theoretical pore size diameter of 14 Å.[25] The difference is probably reasoned by restricted applicability of density functional theory (DFT) calculations for micropores.[33,35] There are also some pores with diameters larger than 2.5 nm, which cannot be ascribed to the diameter of the MOF pores but effects such as defects in the MOF structure, interparticle porosity, and morphology. Given the fact that almost 90% of the cumulative pore volume arises from pores smaller than 2 nm, it can be assumed that the MOF was successfully activated.

Another useful analytical method to investigate the uptake of Mg ions into the MOF is scanning electron microscopy (SEM) together with energy-dispersive spectroscopy (EDS) in order to show the areal distribution of elements in the material and combine this to a visualization of the MOF crystals. The SEM images show hexagonal rods of 10–20 µm length (**Figure 3**a). High crystallinity, which is shown by the reflections in PXRD and the uniform hexagonal shape of crystals fitting to the hexagonal space group, indicates that these rods are mostly single crystalline. After impregnation, only particles with the same shape as the original Mg-MOF-74 particles are observed (see Figure S1–S3, Supporting Information), indicating that the impregnated salts did not crystallize on the MOF surface altering the morphology. In addition, EDS of the impregnated MOF particles shows no aal clustering of Cl^-, Br^-, and F^- (Figure 3b–d), what could be the case if MgX_2 ($X^- = Cl^-$, Br^-, BF_4^-) were not inside the pores but forming phase segregation. Mapping of O and C shows the same intensity distributions (Figure S4, Supporting Information). Uniform distribution for all samples further supports a successful impregnation of Mg-MOF-74 with either $MgCl_2$, $MgBr_2$, or $Mg(BF_4)_2$.

2.2. Conductivity Investigations

Mg-MOF-74 was impregnated according to the aforementioned procedure with MgX_2 ($X^- = Cl^-$, Br^-, BF_4^-) dissolved in PC leading to the formation of Mg-MOF-74 0.4 MgX_2 3.8 PC.

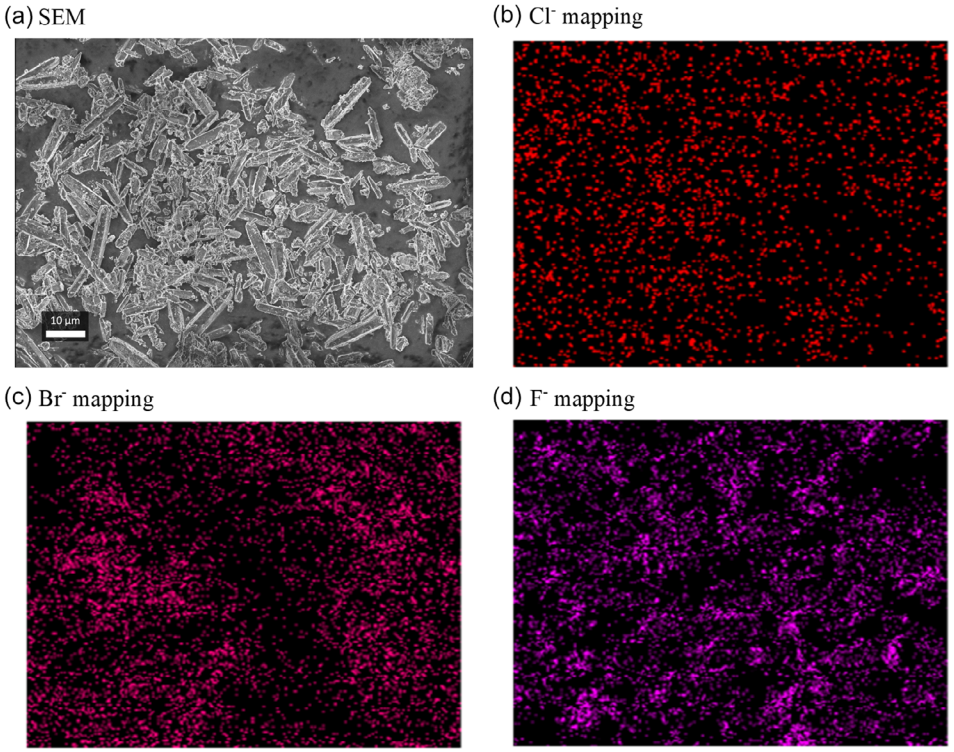

Figure 3. a) SEM image of pure Mg-MOF-74, b) EDS mapping of Cl^-, c) EDS mapping of Br^-, and d) EDS mapping of F^-.

Potentiostatic electrochemical impedance spectroscopy (PEIS) was applied to determine the resistance of the MOF sample and to calculate the total conductivity σ. Nyquist plots of the data show a semicircle at high frequencies followed by a tail at low frequencies. The semicircle can be well ascribed to a resistor (R) and a capacitor (Q) in parallel and be fitted with a RQ model reflecting the ionic conduction across the sample, whereas the low-frequency tail is attributed to a constant phase element (CPE) generated by the blocking behavior of the stainless steel electrodes. Analysis of PEIS data gives room temperature ionic conductivities of $\sigma(298\,°C) = 3.4 \times 10^{-5}\,S\,cm^{-1}$ for $MgBr_2$·PC@Mg-MOF-74, $\sigma(298\,°C) = 5.0 \times 10^{-5}\,S\,cm^{-1}$ for $MgCl_2$·PC@Mg-MOF-74, and $\sigma(298\,°C) = 6.2 \times 10^{-5}\,S\,cm^{-1}$ for $Mg(BF_4)_2$·PC@Mg-MOF-74 (**Figure 4**a), whereas pure Mg-MOF-74 showed insulating behavior, indicated by scattered data in the Nyquist plot (Figure S5, Supporting Information). The (mean) electric mobility of Mg^{2+} ions is $u(298\,K) = 1.7\,10^{-7}$, 4.2, and $5.1\,cm^2\,V^{-1}\,s^{-1}$ for the different combinations $MgBr_2$·PC@Mg-MOF-74, $MgCl_2$·PC@Mg-MOF-74, and $Mg(BF_4)_2$·PC@Mg-MOF-74, respectively. This high mobility of Mg^{2+} competes well with the one of Li^+ in state-of-the-art solid electrolytes even though Mg^{2+} is double charged.[36] Arrhenius plots of temperature-dependent PEIS measurements show low activation energies for the ionic conductivity of $E_a = 0.24\,eV$ for $MgBr_2$·PC@Mg-MOF-74, $E_a = 0.22\,eV$ for $MgCl_2$·PC@Mg-MOF-74, and $E_a = 0.20\,eV$ for $Mg(BF_4)_2$·PC@Mg-MOF-74 (Figure 4b). Utilization of the salt $Mg(BF_4)_2$ leads to the highest conductivity observed, probably due to delocalization of the charge within BF_4^-. Full dissociation of MgX_2 is more likely for BF_4^-. Hence, Mg^{2+} is more mobile and the total conductivity is higher for BF_4^- than for the other investigated halide anions.

Arrhenius-like behavior is found over a wide temperature range of 233–333 K with a high r-square value of at least 0.97 or higher. This shows that the conductivity mechanism corresponds rather to a crystalline solid-state material than to a liquid or glassy material. This is contrary to the case of ionic liquid-loaded MOFs, which show more the typical curved line in the Arrhenius plot characteristic for viscous liquids.[13] Counterintuitively, the conductivity above 313 K shows a downside deviation from pure Arrhenius behavior, instead of an upside deviation expected due to higher fluidity usually observed for liquid electrolytes. This may be a result of the capillary effect whose opposite acting force enlarges by higher motion.

Instead of the Arrhenius model, conductivity could also be described by the Vogel–Fulcher–Tammann (VFT) model.[37–39] VFT was first developed to describe polymer electrolytes but is also used to describe ionic liquid-loaded MOFs.[28] Plotting the data shown in Figure 4b according to VFT equation instead of Arrhenius equation shows better regression (Figure 4c). This indicates liquid-like behavior to a certain extent. Cooling to room temperature after the activation energy measurements shows similar room temperature ionic conductivities for all samples, proving the stability at low and elevated temperatures in a range of 233–333K. Working at temperatures below RT down to 233 K shows that the electrolyte is able to work under severe frost conditions, as well as it works under moderate heating up to 333K, reversibly. Therefore, the electrolyte is suitable for a wide range

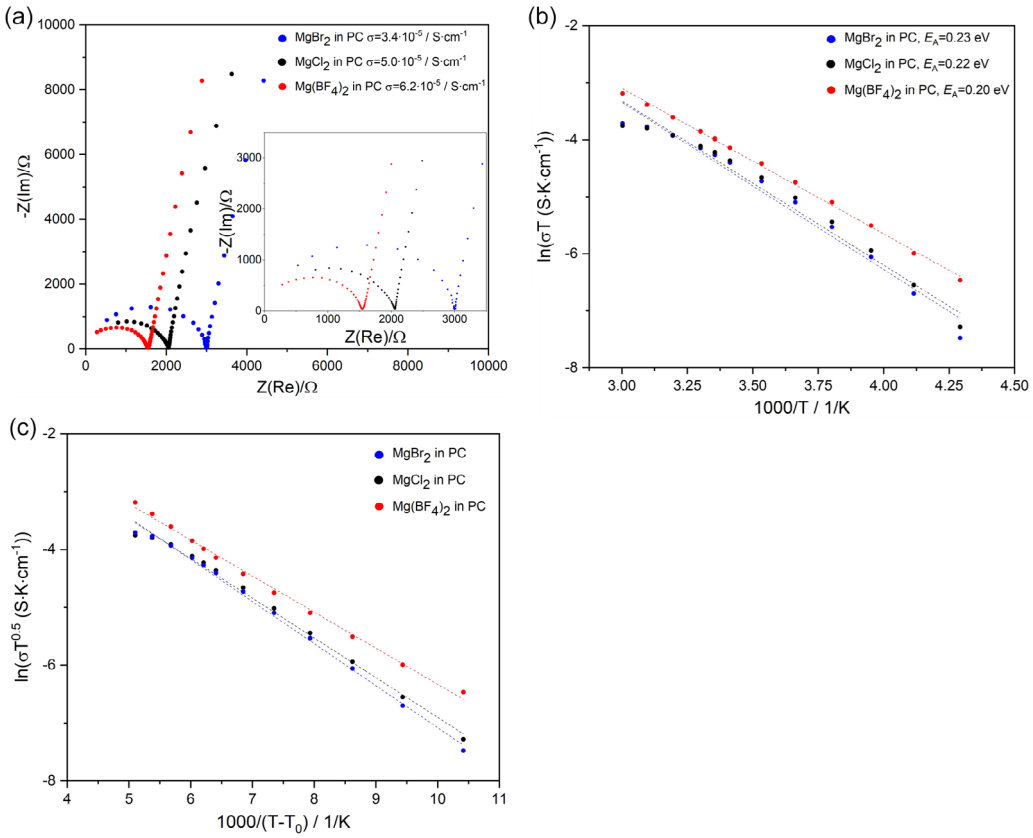

Figure 4. a) PEIS of MgX_2·PC@Mg-MOF-74 ($X^- = Cl^-$, Br^-, BF_4^-); b) Arrhenius plots of MgX_2·PC@Mg-MOF-74 ($X^- = Cl^-$, Br^-, BF_4^-) at temperatures of 233–333 K; and c) VFT plots of MgX_2·PC@Mg-MOF-74 ($X^- = Cl^-$, Br^-, BF_4^-) at temperatures of 233–333 K.

of applications without the need for additional temperature regulation systems. Nyquist plots of each composite show only one semicircle and a capacitive low-frequency tail at each temperature, indicating that the transport mechanism is the same for all samples (Figure S6–S8, Supporting Information).

2.3. Plating/Stripping Behavior and Stability

Plating/stripping experiments were carried out to evaluate the behavior of the MOF electrolytes in electrochemical cells under DC current. A steady, direct current (chronopotentiometry) was applied, and magnesium was stripped from the anode side and plated on the opposite cathode side. The change of potential during these measurements shows the stability of the electrolyte at the given current density. All plating/stripping measurements were performed with the same cell setup steel | Mg foil | MgX_2·PC@Mg-MOF-74 | Mg foil | steel. To evaluate the highest current density for plating/stripping with stable cycling performance, first, the behavior of each MOF electrolyte was investigated at different current densities at 333 K (**Figure 5**a–c). The applied potential remained stable for current densities up to 0.25 μA cm^{-2} while at higher current densities, the potential rose even during an individual polarization step, indicating reactions at the electrodes that increase the resistance. We assume that at higher currents, either an unfavorable solid electrolyte interface (SEI), e.g., a passivation layer between Mg foil and electrolyte is formed, or the electrolyte decomposes at contact with the Mg foil. Therefore, also long time plating/stripping measurements were carried out at $i = 0.25$ μA cm^{-2} (Figure 5d–f).

Plating/stripping over a period of 100 h with 10 h per polarization step shows that $MgBr_2$·PC@Mg-MOF-74 is the most stable material against Mg foil, as the potential growth is slowest and growth also seems to run into saturation. However, altogether, MgX_2·PC@Mg-MOF-74 do not prove to be stable against Mg metal and therefore, a more suitable interface between electrolyte and Mg would be needed. Impedance measurements before and after plating/stripping show only small changes of the first semicircle (Figure S9–10, Supporting Information) and indicate that the electrolyte itself remains stable in contrast to its interface with Mg metal. $Mg(BF_4)_2$·PC@Mg-MOF-74 shows a larger growth of resistance during the plating/stripping measurement (Figure S11, Supporting Information) and a lower stability.

After 40 days with direct contact of Mg foil and electrolyte, cells were opened and a PXRD of the electrolytes was measured (**Figure 6**), and crystalline electrolyte with good accordance to activated Mg-MOF-74 can be seen as result. Consequently, it can be stated that the crystal structure of the MOF remains stable during contact with Mg foil and only the direct interface is affected. To prevent this formation of an apparently insulating SEI and to keep the interface resistance low, an additional interface modification is necessary.

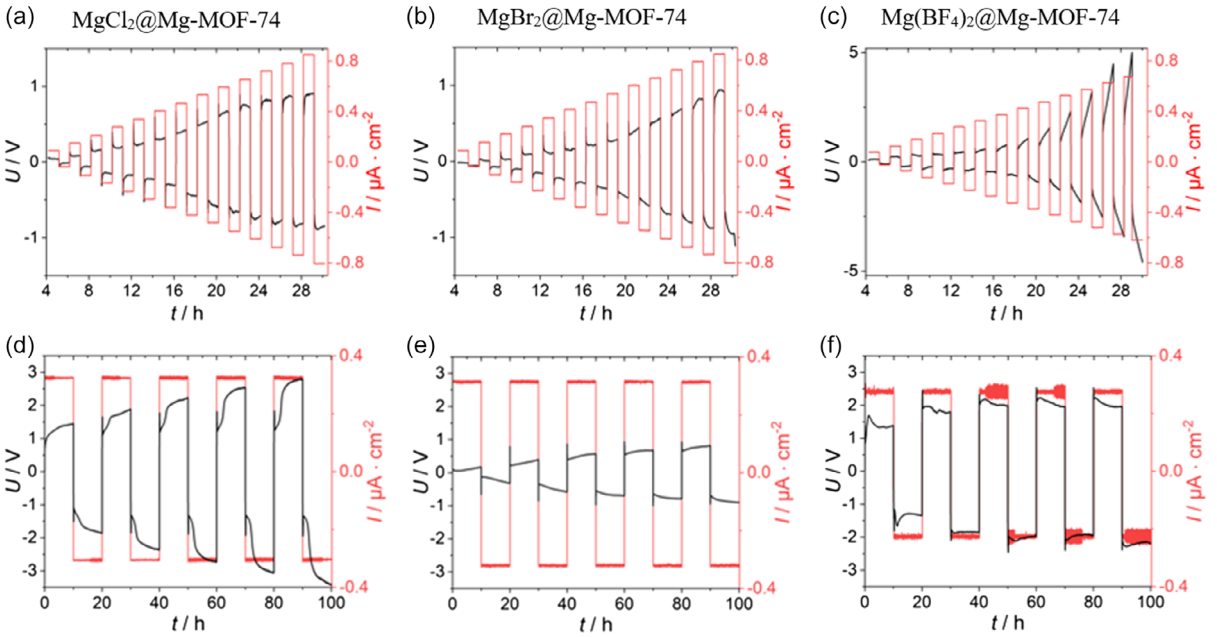

Figure 5. Plating/stripping experiments at different currents at 333 K of MgX_2·PC@Mg-MOF-74 with a) $X = Cl^-$; b) $X = Br^-$; and c) $X = BF_4^-$; plating/stripping experiments at 298 K at 0.25 µA cm^{-2} of MgX_2·PC@Mg-MOF-74 with d) $X = Cl^-$; e) $X = Br^-$; and f) $X = BF_4^-$. All experiments were carried out without previous cycling.

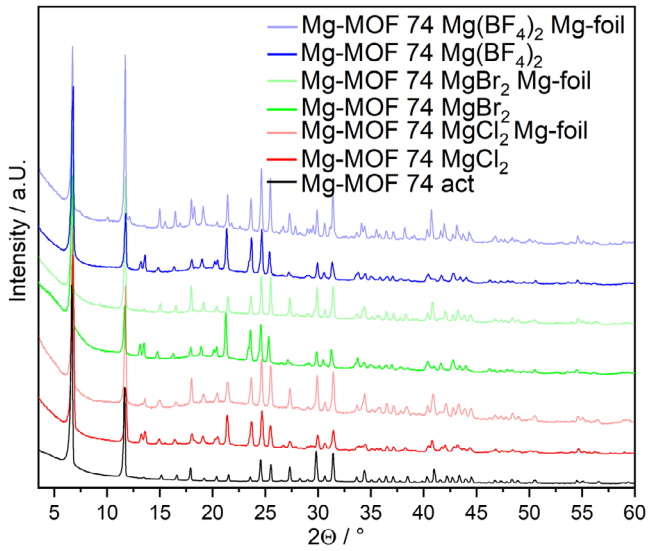

Figure 6. PXRD of different setups of MgX_2@Mg-MOF-74 after contact with Mg foil.

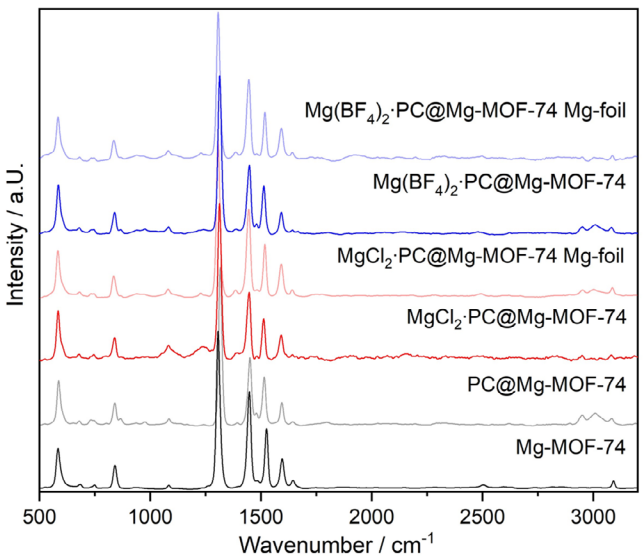

Figure 7. Raman spectra of Mg-MOF-74, Mg-MOF-74 impregnated with PC, MgX_2·PC@Mg-MOF-74 ($X^- = Cl^-$, BF_4^-), and MgX_2·PC@Mg-MOF-74 ($X^- = Cl^-$, BF_4^-) after contact with Mg foil.

Furthermore, elemental analysis of all samples was carried out (Table S1, Supporting Information). Found composition and calculated composition of elements match well. Also, after contact with Mg foil, the composition kept stable according to elemental analysis, indicating that no MOF decomposition is commencing on a larger scale.

To further investigate, if and to which extent the MOF chemically decomposes upon contact with magnesium foil, Raman spectra were recorded of each sample (**Figure 7**). Comparison shows that bands of Mg-MOF-74 dominate the Raman spectra at lower wavenumbers and are assigned specifically in Table S2, Supporting Information.[40] Addition of PC to Mg-MOF-74 leads to additional bands in each impregnated sample at wavenumbers of 2900–3000 cm^{-1}, which can be ascribed to the CH_3 stretching bands of PC. No additional band of Mg-X vibrational modes arise by the addition of MgX_2, indicating that the salts were fully dissolved. However, BF_4^- has vibrational modes by itself; the most

intense band of BF_4^- is at 1050 nm^{-1},[41] where it overlaps with a band of Mg-MOF-74 and is only slightly visible. Cycling measurements with magnesium foil on both sides do not lead to additional bands or vanishing of existing ones, indicating that major decomposition processes can be excluded.

Raman spectra of samples with $MgBr_2$ are shown in the SI only, as bromide absorbs the laser light and emits infrared light which overexposes the Raman detector (Figure S12, Supporting Information), which prevents separated bands from being detectable.

In addition, UV–vis–NIR diffuse reflectance spectra were recorded. They show only minor differences in reflectance for nonimpregnated, impregnated, and also for impregnated samples after contact with magnesium foil (Figure S13, Supporting Information). Main absorption occurs at 350–430 nm which leads to the yellow color of all samples. Other bands are not visible. For the $MgBr_2$-impregnated samples, a second absorption band is visible at about 500 nm being low in intensity compared to the main absorption band, so that it does not affect the yellow appearance. However, this band overlaps with the wavelength of the laser used for Raman spectroscopy (532 nm) resulting in an excitation of bromide ions and emission of infrared light, which overexposes the Raman detector.

Furthermore, the onset potential for oxidation of the different MOF electrolytes was investigated with linear sweep voltammetry (LSV) at room temperature from open cell voltage (OCV, no voltage applied) to 5 V in an asymmetric cell with stainless steel as current collector and Mg foil as counter and reference electrode (**Figure 8**). The scan rate was 0.1 mV S^{-1}. The LSV curves confirm that the electrolyte does not form a stable interface with magnesium metal at applied voltages, for the onset potential is about 1–2 V for electrolytes with $MgCl_2$ and $MgBr_2$, and $Mg(BF_4)_2$ is not even stable against Mg metal at OCV.

2.4. Determination of Transference Numbers

The determination of the type of charge carrier is crucial for battery applications of electrolytes. The transference number of a specific ion accounts for the fraction of charge carried by this ion with values between 0 and 1, with a transference number of 1 indicating that all charge is carried by this specific ion. High cation transference numbers are highly favorable, as they suppress electrolyte polarization and prevent dendrite formation and therefore lower the internal resistance and enhance lifetime of batteries.[42] One method to achieve information about the fraction of current carried by magnesium ions is to put foils of magnesium on both sides of the electrolyte. Direct current is applied (chronoamperometry, CA) and the stationary fraction of steady-state current compared to the initial current gives information on the transference number (Equation (4)). CA measurements were carried out, even though it was not possible to achieve a true steady state due to the instability of the electrolytes against magnesium metal. Currents were recorded at different times for the calculation of transference numbers in order to reflect that reaching the steady state of diffusion will be overlayed by ongoing passivation layer formation. A decay time of 1 h was chosen in order to compare the results to similar experiments (Figure S14, Supporting Information),[14,22,23,43,44] The data at 4 h decay time already indicate low slopes and 20 h decay time are depicted as well, as here current decay is fully dominated by passivation layer formation. A waiting step of two hours was added after preparation of each cell.

After 4 h of CA measurement (**Figure 9**), transference numbers were calculated according to the Vincent–Evans method (Equation (4))[45] for $MgCl_2$·PC@Mg-MOF-74, with $t_{Mg^{2+}} = 0.50$, for $MgBr_2$·PC@Mg-MOF-74, with $t_{Mg^{2+}} = 0.76$, and for $Mg(BF_4)_2$·PC@Mg-MOF-74, with $t_{Mg^{2+}} = 0.22$. To the best of our knowledge, a transference number of $t_{Mg^{2+}} = 0.76$ in MOFs is the highest observed value compared to $t_{Mg^{2+}} = 0.47$ and $t_{Mg^{2+}} = 0.41$ reached by group of Sadakiyo.[22,23] Transference numbers calculated after only 1 h are even higher, as in case of $MgBr_2$·PC@Mg-MOF-74, the loss of current is negligible (Figure S14, Supporting Information). After 1 h of CA measurement, transference numbers are $t_{Mg^{2+}} = 0.80$ for $MgCl_2$·PC@Mg-MOF-74, $t_{Mg^{2+}} = 0.96$ for $MgBr_2$@Mg-MOF-74, and $t_{Mg^{2+}} = 0.40$ for $Mg(BF_4)_2$·PC@Mg-MOF-74. However, these values need to be considered with caution as they do not represent a steady state and drop over time. The highest observed transference number for magnesium after 20 h of CA measurement (**Figure 10**) was achieved for the electrolyte $MgBr_2$·PC@Mg-MOF-74 with a value as high as $t_{Mg^{2+}} = 0.45$, which also exhibited the highest stability during long time plating/stripping experiments, followed by $MgCl_2$·PC@Mg-MOF-74 with $t_{Mg^{2+}} = 0.25$ and $Mg(BF_4)_2$·PC@Mg-MOF-74 with $t_{Mg^{2+}} = 0.13$.

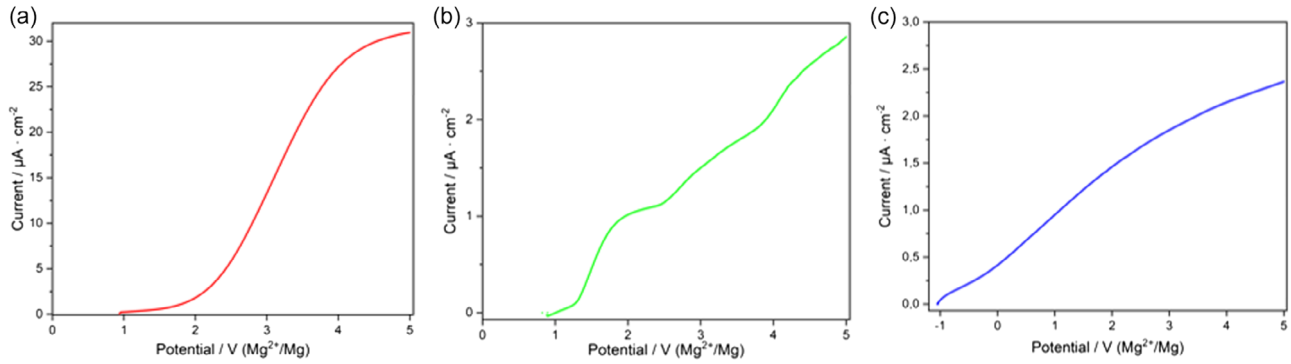

Figure 8. LSV curve of a) $MgCl_2$ (red), b) $MgBr_2$ (green), and c) $Mg(BF_4)_2$ (blue) @Mg-MOF-74.

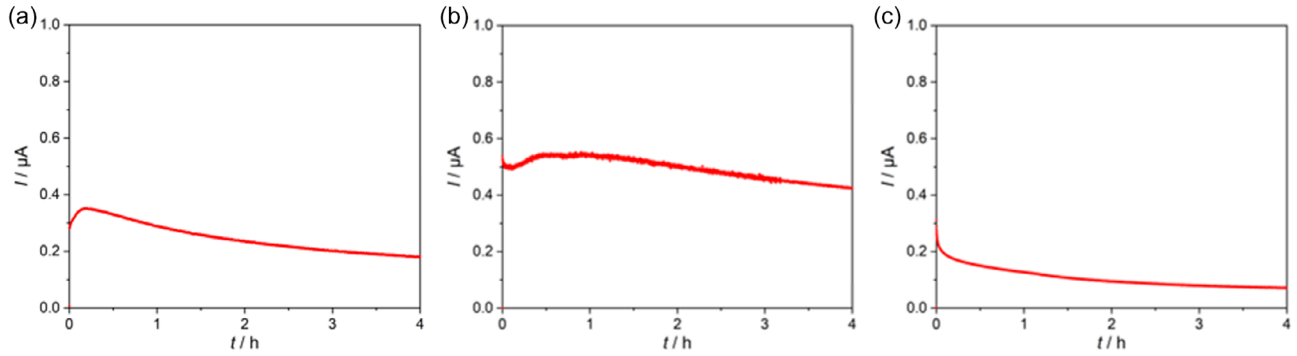

Figure 9. CA measurements of 4 h of a) $MgCl_2$, b) $MgBr_2$, and c) $Mg(BF_4)_2$@Mg-MOF-74.

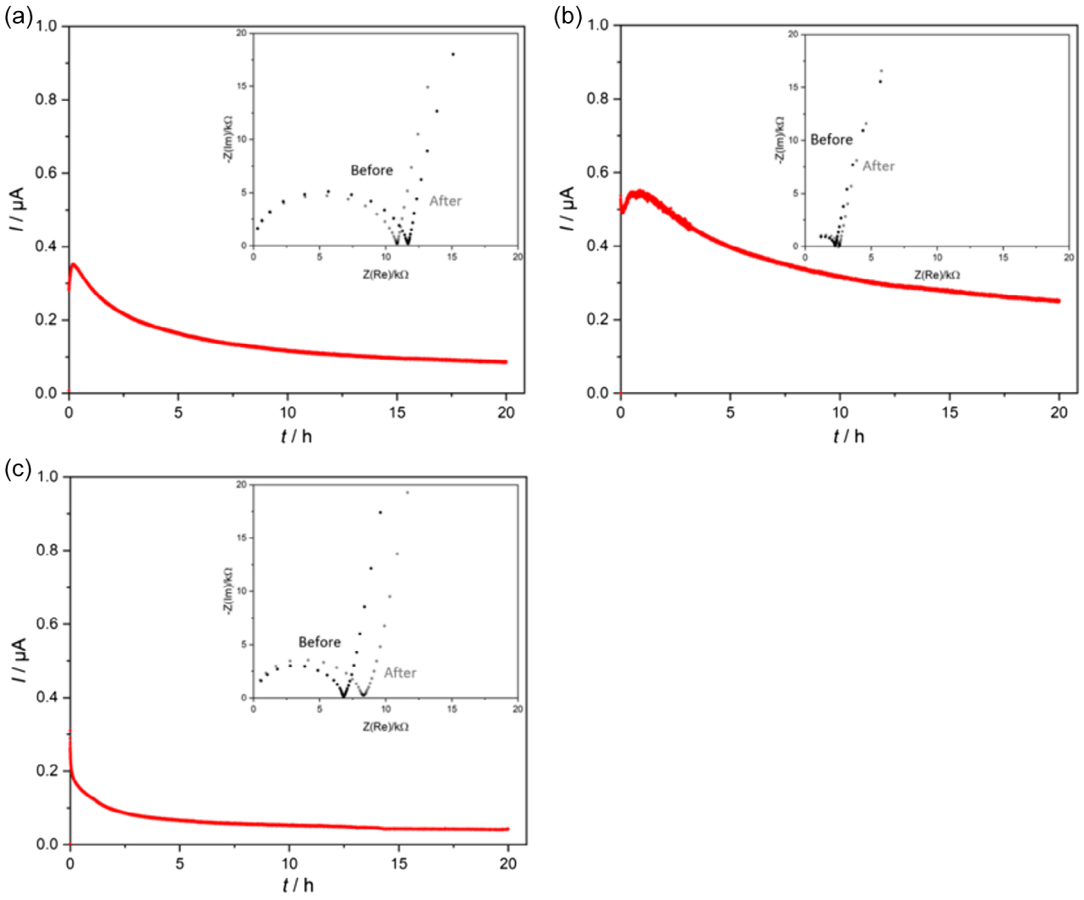

Figure 10. CA measurements of 20 h with a Nyquist plot as inset, measured before and after CA of a) $MgCl_2$, b) $MgBr_2$, and c) $Mg(BF_4)_2$@Mg-MOF-74.

In conclusion, it can be stated that transference numbers of Mg^{2+} even after 20 h CA measurement are at the level of the recently published $t_{Mg^{2+}} = 0.41$ for MIL-101[22] and corroborate the value of $t_{Mg^{2+}} = 0.47$ just published for MOF-74,[23] keeping in mind that the determination of the transference numbers of these examples in the literature was conducted after only 1 h CA and not for longer measurement times. Nyquist plots over the full range before and after 20 h of CA measurement are shown in Figure S15–S17, Supporting Information. The different properties of the anions concerning radii and softness seem to be dominated by the influence of stability of the resulting electrolyte. The salt $MgBr_2$ leads to the most stabile electrolyte and had the lowest conductivity of the three investigated anions. It also leads to the highest transference number, whereas $Mg(BF_4)_2$·PC@Mg-MOF-74 with the highest conductivity but highest passivation had the lowest transference number. So, for these composite electrolytes, the experiments conducted show that electrochemical stability is more important than mere conductivity.

To further examine the formed passivation layer, fourier-transform infrared spectroscopy (FTIR) spectra were recorded of the Mg foils after contact with MgX_2·PC@Mg-MOF-74 ($X^- = Cl^-$, Br^-, BF_4^-) after the CA measurements as well as from a freshly polished Mg foil and from pure Mg-MOF-74 with PC (Figure S18, Supporting Information). The different anions in the electrolyte do not seem to have an influence on FTIR spectra, instead spectra of all cycled foils look alike the pure Mg foil with additional bands that can be assigned to Mg-MOF-74.

For comparison, also the transference number of Mg^{2+} for liquid PC with dissolved $Mg(BF_4)_2$ was determined (**Figure 11**). PC with the same concentration of $Mg(BF_4)_2$ as in MgX_2·PC@Mg-MOF-74 ($X^- = Cl^-$, Br^-, BF_4^-) was chosen, as it dissolves fully in PC in contrast to $MgBr_2$ and $MgCl_2$. The transference number in this liquid electrolyte of Mg^{2+} is 0.12, which is slightly lower than without embedding the electrolyte in the MOF pores. Consequently, this experiment showed that Mg-MOF-74 enhances the transference number of the liquid electrolyte PC, even though the liquid electrolyte is embedded in a solid host. Unfortunately, the improvement of transference number is only small, as also in this case, an insulating SEI is formed. $Mg(BF_4)_2$ accelerates passivation layer formation, which is also the case for this measurement.

As pointed out before, $MgBr_2$·PC@Mg-MOF-74 has highly promising values for transference numbers but the issue with its low stability versus Mg metal cannot be neglected. Still, these promising results show that $MgBr_2$@Mg-MOF-74 could be used as a highly selective Mg^{2+}-ion conductor together with a stable interface against magnesium.

2.5. Computational Investigation

In order to elaborate on the experimental findings, computational investigations were carried out (DFT, see Experimental Section for details). As the nature of the transported charge carrier is not known, combinations of Mg^{2+} with the different anions of the used Mg salts and the solvent were addressed.

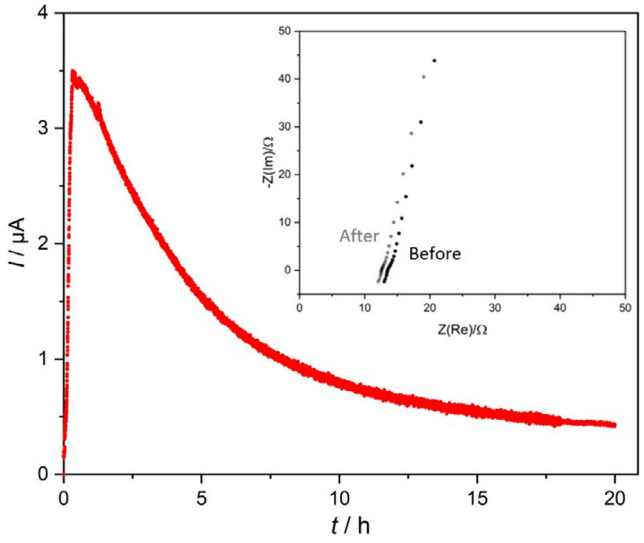

Figure 11. CA measurements of PC with dissolved $Mg(BF_4)_2$ for 20 h with a Nyquist plot as inset recorded before and after CA.

Table 1. The Gibbs energies for the formation ΔG_{form} of the Mg compounds from Mg^{2+}, Cl^-, Br^-, BF_4^-, and PC are presented. The systems are grouped together according to their counterion, with alternating grey and white backgrounds to enhance the visibility. The most stable neutral compound with a Mg and a binding partner in a group is always green, while the most stable charged complex is highlighted in yellow. The Gibbs energies are calculated at the PBE0-D3(BJ)/def2-TZVP (COSMO) level of theory with a temperature of 298.15 K.

Complex	ΔG_{form} [kJ mol^{-1}]	Complex	ΔG_{form} [kJ mol^{-1}]
$MgPC^{2+}$	−41.2	$Mg(PC)_2Br_2$	−159.1
$Mg(PC)_2^{2+}$	−61.9	$Mg(PC)_3Br_2$	−151.0
$Mg(PC)_3^{2+}$	−86.4	$Mg(PC)_4Br_2$	−129.0
$Mg(PC)_4^{2+}$	−100.2	$MgBr^+$	−86.2
$Mg(PC)_5^{2+}$	−122.9	$MgPCBr^+$	−107.7
$Mg(PC)_6^{2+}$	−121.9	$Mg(PC)_2Br^+$	−119.6
$MgCl_6^{4-}$	−128.5	$Mg(PC)_3Br^+$	−127.1
$MgCl_2$	−188.8	$Mg(PC)_4Br^+$	−133.4
$MgPCCl_2$	−198.6	$Mg(PC)_5Br^+$	−129.3
$Mg(PC)_2Cl_2$	−205.6	$Mg(BF_4)_6^{4-}$	−35.5
$Mg(PC)_3Cl_2$	−185.6	$Mg(BF_4)_2$	−68.5
$Mg(PC)_4Cl_2$	−169.6	$MgPC(BF_4)_2$	−91.0
$MgCl^+$	−110.2	$Mg(PC)_2(BF_4)_2$	−108.2
$Mg(PC)Cl^+$	−132.1	$Mg(PC)_3(BF_4)_2$	−121.9
$Mg(PC)_2Cl^+$	−144.3	$Mg(PC)_4(BF_4)_2$	−127.0
$Mg(PC)_3Cl^+$	−151.3	$MgBF_4^+$	−45.2
$Mg(PC)_4Cl^+$	−148.5	$MgPCBF_4^+$	−68.8
$Mg(PC)_5Cl^+$	−150.2	$Mg(PC)_2BF_4^+$	−89.6
$MgBr_6^{4-}$	−59.4	$Mg(PC)_3BF_4^+$	−106.2
$MgBr_2$	−141.0	$Mg(PC)_4BF_4^+$	−119.6
$MgPCBr_2$	−152.4	$Mg(PC)_5BF_4^+$	−121.5

Table 1 presents the Gibbs energies for the formation ΔG_{form} of various complexes with Mg^{2+}, PC and Cl^- or Br^- or BF_4^-. All optimized structures are shown in **Figure 12** and Figure S19, Supporting Information. According to the calculated Gibbs energies of formation, the compound $Mg(PC)_2Cl_2$ is energetically most favorable for the counter ion Cl^-. As $Mg(PC)_2Cl_2$ is neutral, it does not move through the MOF when a voltage is applied. The sixth most energetically favorable compound, $Mg(PC)_3Cl^+$, is the first charged complex. In order to reach this charged complex $Mg(PC)_3Cl^+$, an energy of +54.3 kJ mol^{-1} must be overcome. The Gibbs energies for the complex formation with the Br^- counter ion show also that the neutral compound $Mg(PC)_2Br_2$ is energetically most favorable. To form the most energetically favorable charged complex $Mg(PC)_4Br^+$, an energy +25.7 kJ mol^{-1} must be applied, which is half as much as for the Cl^- counter ion.

Although the Gibbs energies for complex formation with the BF_4^- counterion give a qualitatively similar picture to the counterions Cl^- and Br^- with the energetically most favorable neutral compounds $Mg(PC)_4(BF_4)_2$, only an energy of 5.5 kJ mol^{-1} is

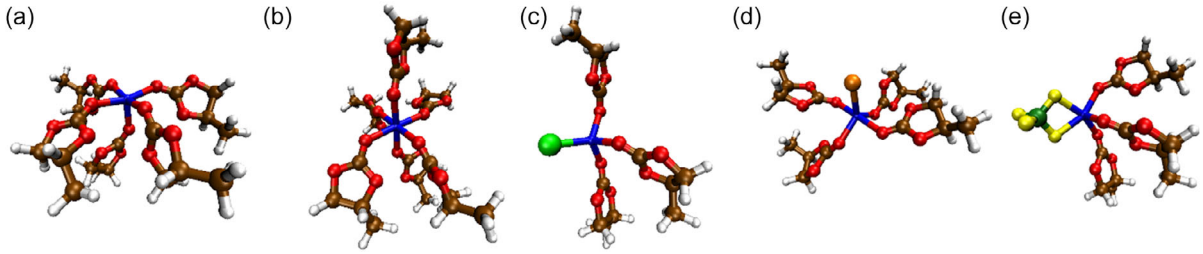

Figure 12. Structures of a) $Mg(PC)_5^{2+}$, b) $Mg(PC)_6^{2+}$, c) $Mg(PC)_3Cl^+$, d) $Mg(PC)_4Br^+$, and e) $Mg(PC)_5BF_4^+$. Calculations are performed at the PBE0-D3(BJ)/def2-TZVP (COSMO) level of theory. Color scheme for the atom types: white, red, brown, blue, light green, dark green, orange, and yellow spheres denote H, O, C, Mg, Cl, B, Br, and F, respectively.

required to achieve the energetically most favorable charged complex $Mg(PC)_5BF_4^+$. Assuming chemical equilibrium between $Mg(PC)_4(BF_4)_2$ and $Mg(PC)_5BF_4^+$, 8% of the charged complex would be present in solution. In order to achieve the doubly charged charge carriers $Mg(PC)_5^{2+}$ and $Mg(PC)_6^{2+}$, starting from the neutral $Mg(PC)_4(BF_4)_2$ compound, an energy of only 4.1 or 5.1 kJ mol^{-1} is required. These would be even more energetically favorable than the singly charged complex $Mg(PC)_5BF_4^+$. The Gibbs energy differences between $Mg(PC)_5BF_4^+$, $Mg(PC)_5^{2+}$, and $Mg(PC)_6^{2+}$ are 1 kJ mol^{-1} and less. These energy differences are below chemical accuracy, and lower than the accuracy that can usually be achieved using standard quantum chemical methods. Therefore, the three complexes can be considered to be energetically equivalent within the accuracy of the applied method.

As the least amount of energy is required to form charged compounds with BF_4^-, the lowest activation energy is expected for this counterion, the highest activation energy for the complex with the counterion Cl^-. This finding is consistent with the experimental results. The Gibbs energy for the formation of the charge carriers correlates with the experimental activation energies. It should be noted, however, that in principle the activation energies differ very little in the experiment.

The results also show one possible contributing for the high ion conductivity observed in the presence of the BF_4^- counterion. The energetic observation suggests that in addition to the singly charged complexes, doubly charged charge carriers are also formed. In the case of the counterions Cl^- and Br^-, only the singly charged charge carriers are energetically favored.

The partial charge (Table S3, Supporting Information) at the Mg ion increases in the analyzed complexes and compounds when changing from Cl^- to Br^- to BF_4^-. This phenomenon is to be expected as a consequence of the increasing size of the counterions, which may be a contributing factor to the easier formation of charged species for Br^- and, to a greater extent, for BF_4^-.

Subsequently, we conducted an investigation of the energetically favored singly positively charged complexes $Mg(PC)_3Cl^+$, $Mg(PC)_4Br^+$, and $Mg(PC)_5BF_4^+$ and the doubly charged complex $Mg(PC)_5^{2+}$ in the MOF structure. First, the calculations show that these compounds all fit geometrically well into the MOF pores (see **Figure 13** and Figure S20, Supporting Information). Second, **Table 2** illustrates that the calculated binding energies follow the order $Mg(PC)_3Cl^+$@MOF < $Mg(PC)_4Br^+$@MOF < $Mg(PC)_5BF_4^+$@MOF < $Mg(PC)_5^{2+}$@MOF, indicating that the $Mg(PC)_3Cl^+$ complex exhibits the weakest interaction with the MOF. However, it is noteworthy that the medium- and long-range dispersion interactions, arising from the different numbers of PC ligands, significantly impact the binding energy between the compounds and the MOF. To elucidate the contribution of medium- and long-range dispersion interactions, we further calculate the binding energies without considering the dispersion correction D3. The resulting binding energy order is as follows $Mg(PC)_5BF_4^+$@MOF < $Mg(PC)_3Cl^+$@MOF < $Mg(PC)_4Br^+$@MOF < $Mg(PC)_5^{2+}$@MOF. The compound with the largest medium- and long-range dispersion interaction and the weakest ionic interaction between the complex and the MOF pores indicates that the flattest potential landscape is to be expected. Thus, it can be reasonably assumed that the lowest barrier for migration will be observed in the case of the complex $Mg(PC)_5BF_4^+$ compared to $Mg(PC)_3Cl^+$@MOF and $Mg(PC)_4Br^+$@MOF.

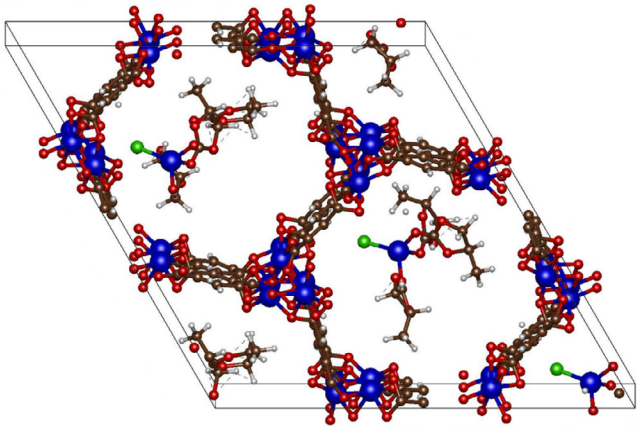

Figure 13. The structural model for $Mg(PC)_3Cl^+$@MOF, as determined at PBE-D3/pw (PAW P) level of theory, is presented herewith. The spheres depicted in white, red, brown, blue, and light green represent the atoms H, O, C, Mg, and Cl, respectively.

In addition to the binding energy analysis, our Bader charge analysis (see Table 2) reveals that the MOF acts as an electron withdrawer in systems $Mg(PC)_3Cl^+$@MOF and $Mg(PC)_4Br^+$@MOF, while it serves as an electron donator in systems $Mg(PC)_5BF_4^+$@MOF and $Mg(PC)_5^{2+}$@MOF. These results imply an electrostatic repulsion interaction between the

Table 2. The binding energy with/without dispersion interaction and Bader charge for the complexes inside the MOF structure. The supercell of the MOF structures comprises three complexes.

Systems	Binding energy (with/without dispersion) [eV/complex]	Bader charge [*e*]			
		MOF	Per complex	Per anion	Per Mg
$Mg(PC)_3Cl^+$@MOF	–7.84/–6.41	–0.36	1.12	–0.69	1.68
$Mg(PC)_4Br^+$@MOF	–8.46/–6.62	–1.08	1.36	–0.46	1.69
$Mg(PC)_5BF_4^+$@MOF	–8.64/–6.18	0.12	0.96	–0.93	1.72
$Mg(PC)_5^{2+}$@MOF	–17.15/–14.84	0.24	1.92	–	1.71

$Mg(PC)_5BF_4^+$ compound and the MOF due to a positive partial charge on both. Specifically, the BF_4^- anion exhibits a stronger ability to keep electrons compared to Cl^- and Br^-, facilitating electron transfer from the MOF to the compound. Notably, this transfer of electrons can amount to up to 1.08 electrons per three $Mg(PC)_4Br^+$ to the MOF, resulting in a pronounced electrostatic attraction between the two entities. This finding further supports the experimental observation of high transference numbers for $MgBr_2$·PC@Mg-MOF-74 and second highest for $MgCl_2$·PC@Mg-MOF-74. The Bader charge for the investigated systems shows an interesting correlation to the transfer rate. The geometric structures of the complexes in the MOF, as illustrated in Figure S20, Supporting Information, demonstrate that the small anions Cl^- and Br^- of the $Mg(PC)_3Cl^+$ and $Mg(PC)_4Br^+$ point toward the Mg of the MOF. The doubly charged $Mg(PC)_5^{2+}$ exhibits binding energies that are twice as high as those of the singly charged complexes. This indicates that transfer rates per complex should be lower compared to the singly charged complexes.

In summary, our investigations, including binding energy calculations and Bader charge analysis, are consistent with the experimental observations. They indicate why $Mg(PC)_5BF_4^+$ may give the lowest activation energy within the MOF and why $Mg(PC)_4Br^+$ can have the highest transference numbers within the MOF.

3. Conclusion

In this work, a MOF-based, quasi-solid-state Mg-ion conductor was achieved by combination of Mg-MOF-74 together with PC and different fundamental magnesium salts constituted from halides and pseudo-halides MgX_2 ($X = Cl^-$, Br^-, BF_4^-). The influence of the different anions on the overall conductivity and other electrochemical parameters, as well as the nature of the charge carrier was investigated experimentally and by DFT computational studies. The combined study reveals a dualism between very good electrochemical parameters and a charge carrier dependent lack of stability vs. Mg metal as electrode material. Altogether, a quasi-solid-state Mg-ion conductor with high room temperature conductivity of $\sigma = 0.6 \times 10^{-4}\,S\,cm^{-1}$ was synthesized that shows Arrhenius type behavior of conductivity over a wide temperature range from 233 to 333 K. Thereby, the presented electrolyte exhibits good conductivity even at low temperatures such as room temperature and hence is applicable without the need of additional heating. Also, a VFT plot is shown to get an even better fit above 313 K. The system acts like a quasi-solid electrolyte that exhibits remarkably low activation energies of only 0.20 eV. The stability of MOF-74 against Mg foil was investigated. A resistive passivation layer is formed, leading to low current densities in DC experiments due to a thin layer elusive for analytical investigations that indicate the MOF to be otherwise intact. The interface was investigated with XRD, elemental analysis, Raman, and FTIR, but no changes of the composite electrolyte were detected due to the small thickness of this layer. In an attempt to determine transference numbers of each composite, problems to achieve a steady state were encountered indicating passivation layer formation. Still, transference numbers of Mg up to $t_{Mg^{2+}} = 0.45$ for $MgBr_2$·PC@Mg-MOF-74 were determined subsequent to passivation layer formation that prove conductivity of Mg^{2+} ions. It was shown that the initial transference numbers determined after 4 h of measurement are even as high as $t_{Mg^{2+}} = 0.76$, which further indicate opportunities of this system as potential quasi-solid-electrolyte even together with simple and fundamental Mg salts. Comparison of the hybrid MOF electrolyte with pure PC as reference system showed that the transference number of $Mg(BF_4)_2$·PC@Mg-OF-74 is higher than of the liquid electrolyte PC itself. So, the MOF is not only a solid host material for liquid electrolytes, but it can also enhance its electrochemical properties. Computational DFT studies of the complexes in solution (modeled with a solvent model) have revealed a correlation between the activation energy for Mg-ion migration through the MOF and the Gibbs energy required to form charged Mg complexes in solution. The calculations presented indicate that the order of the Gibbs energy of formation to build a charged species from the lowest to highest is $Mg(BF_4)_2 < MgBr_2 < MgCl_2$. In the case of $Mg(BF_4)_2$, the calculations indicate the formation of singly ($Mg(PC)_5BF_4^+$) and doubly ($Mg(PC)_5^{2+}$ and $Mg(PC)_6^{2+}$) charged species. In contrast, for $MgBr_2$ and $MgCl_2$, only the formation of singly charged species ($Mg(PC)_3Cl^+$, $Mg(PC)_4Br^+$) is expected. The DFT calculations of the complexes within the MOF pore demonstrate that the most stable charged Mg species found computationally fit geometrically well into the MOF pores. Furthermore, the investigation of different charged compounds within the MOF structure reveals variations in the binding energy and charge transfer. Consequently, the binding energies (with and without long-range dispersion interaction) between the MOF pore and the singly positively charged complexes with the anions Cl^-, Br^- and BF_4^- indicate that the $Mg(PC)_5BF_4^+$ may have the lowest activation energy. The change in the calculated Bader charge of the various charged compounds and the MOF

correlates with the experimental transference numbers. The experimental stability study showed an influence of the anions on the passivation layer formation, and Br^- could be identified to lead to the most stable electrolyte. We conclude that $MgBr_2$·PC@Mg-MOF-74 has promising electrochemical properties for a Mg^{2+}-ion conductor due to the low activation energy and good conductivity even at room temperature. $MgBr_2$·PC@Mg-MOF-74 would highly benefit from a stable interface and result in a single ion conductor, as the high initial transference number of almost 0.8 indicates.

4. Experimental Section

Synthesis of Mg-MOF-74: 2560 mg $Mg(NO_3)_2$·6 H_2O were dissolved in 40 mL water and 960 mg 2,5-dihydroxyterephtalic acid were dissolved in absolute ethanol. Both solutions were heated, after dissolution combined and stirred for 30 min under reflux at an oil bath temperature of 100 °C. 800 mg NaOH solved in 3 mL water were added leading to an immediate precipitation of a yellow solid. After further stirring at reflux for 20 h, the solution cooled down to room temperature. The precipitate was collected by filtration, washed several times with water and ethanol, and dried under reduced pressure. To confirm formation of Mg-MOF-74, PXRD was carried out on the product.

Activation: To empty the pore system before implementing Mg^{2+} and PC and to get rid of water and ethanol as proton donating solvents, 1 g Mg-MOF-74 was soaked in 20 mL methanol for a week under daily exchange of methanol. After solvent exchange, methanol was decanted and the MOF was predried slowly under argon at an elevated temperature. Afterward, it was further dried under continuous vacuum ($p < 0.1$ Pa) for 24 h at 200 °C. To confirm activation, the BET surface area of the activated MOF was determined, as well as further PXRD was carried out to secure that no change in the crystal structure occurred.

Impregnation: 37.5 mg (0.155 mmol) activated Mg-MOF-74, 0.065 mmol MgX_2 ($X = Cl^-$, Br^-, BF_4^-) and 0.12 mL (0.589 mmol) PC were mortared in an argon-filled glove box, transferred into an ampoule and sealed. The ampoule was put in an oven for 7 d at 80 °C; warming up and cooling down took 1 h each. Afterward, the ampoule was opened in a glove box to obtain the impregnated product powder.

Characterization: The PXRD patterns were acquired from a PANalytical Empyrean powder diffractometer using Cu Kα radiation ($\lambda = 1.541$ Å) in Bragg–Brentano geometry. N_2 physisorption was measured with a model Autosorb-1 of Quantachrome instruments and was analyzed using ASiQwin software. The surface area was determined using a 5 point BET plot with a correlation coefficient of $r = 0.9999$. Pore size distribution was calculated from the given isotherm via DFT by ASiQwin software as well. The following model assumptions were used: N_2 at 77 K on silica, cylindric pores, and NLDFT equilibrium model. SEM images were gathered with a model Merlin by Zeiss with an acceleration voltage of 3 kV and a current of 100 pA. (EDS analyses were carried out with a XMAX 50 detector from Oxford Instruments with an acceleration voltage of 8 kV and a current of 1 nA. Raman spectroscopy was carried out using a Senterra Raman microscope from Bruker and a 532 nm laser (2 W) as radiation source. FTIR spectroscopy was performed in an Argon-filled glove box on a NICOLET iS 10 FTIR spectrometer from Thermo Fisher Scientific. UV–vis–NIR diffuse reflectance spectra were acquired with a Cary 5000 UV–vis–NIR spectrophotometer and the Cary WinUV Scan Application software (ver. 6.3.0.1595). The instrument was operated in double beam mode with reduced slit height and was equipped with a Praying Mantis Diffuse Reflectance Accessory from Harrick Scientific Products. Elemental analysis for carbon, hydrogen, nitrogen and sulfur (nitrogen and sulfur are not present) was carried out by a UNICUBE from Elementar in tin crucibles.

Impedance Measurements and Conductivity: All conductivity investigations in this work were done with a self-designed cell setup, as described in previous works.[46] All electrochemical measurements were carried out with a VMP 300 electrochemical workstation from Bio-Logic Science Instruments SAS. For the measurements, 70 mg of the quasi-solid electrolyte was put in polyether ether ketone housing with 10 mm diameter and contacted on both sides with stainless steel stamps as blocking electrodes, and a force of 4 Nm was used to fasten the torque to assure contact (≈0.5 MPa). Impedance measurements were carried out in a frequency range of 3MHz–100 mHz with an amplitude of 10 mV. Ionic conductivity was calculated based on Equation (1):

$$\sigma = \frac{1}{R} \cdot \frac{l}{A} \tag{1}$$

where R is the bulk resistance determined from the equivalent circuit in Nyquist plots, l is the thickness of the pellet and A is the area. Unless otherwise noted every measurement was performed at room temperature. Mobility of Mg^{2+} was calculated based on Equation (2):

$$\mu_j = \frac{\sigma}{z \cdot F \cdot c_j} \tag{2}$$

with σ is the ionic conductivity, z is the number of transferred charges, F is the Faraday constant, and c_j the charge carrier concentration. Temperature-dependent measurements were performed in a climate chamber by Weisstechnik in a temperature range from 233 to 333 K with 3 h waiting step for each temperature (6 h waiting step at 233 K). Activation energy (E_A) was calculated according to Arrhenius equation (Equation (3)):

$$\sigma = \frac{\sigma_0}{T} \exp\left(-\frac{E_A}{k_B T}\right) \tag{3}$$

with σ_0 is the conductivity prefactor, k_B is the Boltzmann constant, and T is the absolute temperature. For measurements in transference cell with magnesium foil electrodes (LSV and transference number), a pellet was prepressed at 40 N and a freshly polished Mg foil with a diameter of 9 mm was put either on one or both sides.

Determination of Transference Numbers: Transference numbers were determined with chronoamperometric (CA) measurements by applying a dc potential of 100 mV at the cell. The cell was built up with Mg foil on both sides of the electrolyte: steel | Mg foil | MgX_2@Mg-MOF-74 | Mg foil | steel. Before the actual measurement, a waiting step of two hours was inserted to form an interface between Mg foil and electrolyte. Subsequently, at room temperature, a CA measurement at 100 mV was performed, lasting 20 h to assure that a steady state is reached. Before and after CA, PEIS was carried out.

With these CA investigations, transference number $t_{Mg^{2+}}$ for each Mg salt was calculated with the Vincent–Evans method[45] according to the equation:

$$t_{Mg^{2+}} = \frac{I_{ss}(\Delta V - I_0 R_0)}{I_0(\Delta V - I_{ss} R_{ss})} \tag{4}$$

Therein, I_0, I_{ss}, ΔV, R_0, and R_{ss} represent the initial current, current at steady state, applied voltage, initial resistance, and resistance at steady state.

Computational Details: Calculations of Mg Complexes and Compounds in Solution: The CREST software package was used to create the initial structures of the magnesium complexes and compounds.[47–49] As first step, a conformational search was carried out. Therein the iterative metadynamics with a genetic structure crossing (iMTD-GC) algorithm was applied. In the next step, a structure optimization was performed at the extended tight-binding GFN2-xTB level of theory.[50–52] To include the effects of a possible solvent, the acetonitrile solvent was simulated in these calculations. Therefore, the implicit solvent model analytical linearized Poisson–Boltzmann model was used.[53] The conformer search included conformers up to 125.5 kJ mol^{-1} above the lowest energy structure. The energetically most favorable conformer as well as manually created structures were evaluated on the DFT level of theory. The DFT calculations

were performed with the Turbomole 7.5.1 software package.[54–56] The resolution-of-identity approximation and the "multiple grid" m4 were used in all cases.[57–59] The hybrid density functional PBE0 in combination with the dispersion correction D3(BJ) was applied.[60–66] The solvent PC [relative permittivity $\varepsilon_r = 64$ (rounded from 64.4)][67] was simulated with the implicit conductor-like screening model (COSMO).[68,69] All optimized structures were verified as stationary points by calculating vibrational frequencies at the same level of theory. Therefore, the seminumerical Turbomole script NumForce was used. Furthermore, the vibrational frequencies were used to add the ro-vibrational contribution of the electronic energy, to get the Gibbs energy at the PBE0-D3(BJ)/def2-TZVP (COSMO) level of theory.

A concentration of 1 mol L^{-1} was assumed for all molecules except the solvent. For PC molecules in the solvent PC, a concentration of 11.852 mol L^{-1} was applied. The concentration is included by adding the following correction term to the translational entropy

$$-RT \cdot \ln\left(\frac{V_m^{new}}{V_m^{old}}\right) \tag{5}$$

with the temperature $T = 298.15$ K, the molar gas constant R, and the new (V_m^{new}) and old ($V_m^{old} = 0.02479 m^3 mol^{-1}$) molar volume.

Partial charges are calculated for the molecular system with a Mulliken population analysis.[70]

Computational Details: Calculations of Mg Complexes in the MOF Structure: To investigate the interaction between compounds and MOF, we employed periodic spin-polarized DFT calculations using the Vienna ab initio simulation package.[71–74] The DFT calculations utilized the PBE exchange–correlation functional, based on the generalized gradient approximation, and incorporated also the dispersion correction D3(BJ). A k-spacing of 0.25 $Å^{-1}$ and a cutoff energy of 500 V have been chosen. Electronic self-consistency was achieved with a convergence criterion of 10^{-5} eV, and atomic forces were minimized below 0.01 eV $Å^{-1}$ for relaxed structures. To alleviate the computational demand, we assumed that the adsorption of molecules has a minor influence on the structure of the MOF. Specifically, we kept the structure of the MOF fixed, allowing only the molecules to move in three dimensions during the structure optimization. To further reduce the computational demand, the MOF was presented in two layers along the z-direction with a thickness of about 14 Å, although it is not enough to avoid the interaction between molecules in the z-direction. The average binding energy of molecules within MOF is defined as

$$\Delta E = (E_{total} - E_{MOF} - n \cdot E_{mol})/n \tag{6}$$

where E_{total} is the energy of the optimized structure of molecules adsorbed within MOF, E_{MOF} is the energy of the pure MOF, E_{mol} is the energy of an isolated molecule, and n is the number of molecules inserted into MOF.

Supporting Information

Supporting Information is available from the Wiley Online Library or from the author.

Acknowledgements

Z.W. and J.J. gratefully acknowledge funding by the German Research Foundation (DFG) under Project ID 390874152 (POLiS Cluster of Excellence). R.M. and K.M.-B. gratefully acknowledge the start-up funding of the JLU Giessen. The authors acknowledge computational resources provided by the HPC Core Facility and the HRZ of the Justus-Liebig-University Giessen.

Conflict of Interest

The authors declare no conflict of interest.

Data Availability Statement

The data that support the findings of this study are available from the corresponding author upon reasonable request.

Keywords

activation energy, computational calculations on meta–organic frameworks, ionic conduction, Mg-MOF-74, stability, transference numbers

Received: February 27, 2024
Revised: May 31, 2024
Published online: June 19, 2024

[1] J. Janek, W. G. Zeier, *Nat. Energy* **2016**, *1*, 16141.
[2] M. Mao, T. Gao, S. Hou, C. Wang, *Chem. Soc. Rev.* **2018**, *47*, 8804.
[3] Z. Zhao-Karger, M. E. Gil Bardaji, O. Fuhr, M. Fichtner, *J. Mater. Chem. A* **2017**, *5*, 10815.
[4] Z. Zhao-Karger, R. Liu, W. Dai, Z. Li, T. Diemant, B. P. Vinayan, C. Bonatto Minella, X. Yu, A. Manthiram, R. J. Behm, M. Ruben, M. Fichtner, *ACS Energy Lett.* **2018**, *3*, 2005.
[5] J. Luo, Y. Bi, L. Zhang, X. Zhang, T. L. Liu, *Angew. Chem.* **2019**, *131*, 7041.
[6] H. Yang, N. Wu, *Energy Sci. Eng.* **2022**, *10*, 1643.
[7] S. Ikeda, M. Takahashi, J. Ishikawa, K. Ito, *Solid State Ion.* **1987**, *23*, 125.
[8] Y. Yan, J. B. Grinderslev, M. Jorgensen, L. N. Skov, J. Skibsted, T. R. Jensen, *ACS Appl. Energy Mater.* **2020**, *3*, 9264.
[9] P. Canepa, S. H. Bo, G. Sai Gautam, B. Key, W. D. Richards, T. Shi, Y. Tian, Y. Wang, J. Li, G. Ceder, *Nat. Commun.* **2017**, *8*, 1.
[10] Z. Wang, J. Hu, L. Han, Z. Wang, H. Wang, Q. Zhao, J. Liu, F. Pan, *Nano Energy* **2019**, *56*, 92.
[11] Z. Wang, R. Tan, H. Wang, L. Yang, J. Hu, H. Chen, F. Pan, *Adv. Mater.* **2018**, *30*, 1.
[12] C. Sun, J. H. Zhang, X. F. Yuan, J. N. Duan, S. W. Deng, J. M. Fan, J. K. Chang, M. Sen Zheng, Q. F. Dong, *ACS Appl. Mater. Interfaces* **2019**, *11*, 46671.
[13] W. Xu, X. Pei, C. S. Diercks, H. Lyu, Z. Ji, O. M. Yaghi, *J. Am. Chem. Soc.* **2019**, *141*, 17522.
[14] X. Duan, Y. Ouyang, Q. Zeng, S. Ma, Z. Kong, A. Chen, Z. He, T. Yang, Q. Zhang, *Inorg. Chem.* **2021**, *60*, 11032.
[15] K. Fujie, T. Yamada, R. Ikeda, H. Kitagawa, *Angew. Chem. - Int. Ed.* **2014**, *53*, 11302.
[16] E. M. Miner, M. Dincă, *Philos. Trans. A* **2019**, *377*, 20180225.
[17] T. Chen, S. Chen, Y. Chen, M. Zhao, D. Losic, S. Zhang, *Mater. Chem. Front.* **2021**, *5*, 1771.
[18] R. Zhao, Y. Wu, Z. Liang, L. Gao, W. Xia, Y. Zhao, R. Zou, *Energy Environ. Sci.* **2020**, *13*, 2386.
[19] M. L. Aubrey, R. Ameloot, B. M. Wiers, J. R. Long, *Energy Environ. Sci.* **2014**, *7*, 667.
[20] E. M. Miner, S. S. Park, M. Dincă, *J. Am. Chem. Soc.* **2019**, *141*, 4422.
[21] S. S. Park, Y. Tulchinsky, M. Dincă, *J. Am. Chem. Soc.* **2017**, *139*, 13260.
[22] Y. Yoshida, K. Kato, M. Sadakiyo, *J. Phys. Chem. C* **2021**, *125*, 21124.
[23] Y. Yoshida, T. Yamada, Y. Jing, T. Toyao, K. Shimizu, M. Sadakiyo, *J. Am. Chem. Soc.* **2022**, *144*, 8669.

[24] Z. Wei, R. Maile, L. M. Riegger, M. Rohnke, K. Müller-Buschbaum, J. Janek, *Batter. Supercaps* **2022**, *202200318*, 1.
[25] B. M. Wiers, M. L. Foo, N. P. Balsara, J. R. Long, *J. Am. Chem. Soc.* **2011**, *133*, 14522.
[26] K. Fujie, R. Ikeda, K. Otsubo, T. Yamada, H. Kitagawa, *Chem. Mater.* **2015**, *27*, 7355.
[27] J. M. Tuffnell, J. K. Morzy, N. D. Kelly, R. Tan, Q. Song, C. Ducati, T. D. Bennett, S. E. Dutton, *Dalton Trans.* **2020**, *49*, 15914.
[28] Y. Yoshida, K. Fujie, D. W. Lim, R. Ikeda, H. Kitagawa, *Angew. Chem. - Int. Ed.* **2019**, *58*, 10909.
[29] J. F. Wu, X. Guo, *Small* **2019**, *15*, 1804413.
[30] W. H. Huang, X. M. Li, X. F. Yang, X. X. Zhang, H. H. Wang, H. Wang, *Mater. Chem. Front.* **2021**, *5*, 3593.
[31] P. D. C. Dietzel, R. Blom, H. Fjellvåg, *Eur. J. Inorg. Chem.* **2008**, *2008*, 3624.
[32] W. Guo, Z. Chen, C. Yang, T. Neumann, C. Kübel, W. Wenzel, A. Welle, W. Pfleging, O. Shekhah, C. Wöll, E. Redel, *Nanoscale* **2016**, *8*, 6468.
[33] M. Thommes, K. Kaneko, A. V. Neimark, J. P. Olivier, F. Rodriguez-Reinoso, J. Rouquerol, K. S. W. Sing, *Pure Appl. Chem.* **2015**, *87*, 1051.
[34] Z. R. Herm, J. A. Swisher, B. Smit, R. Krishna, J. R. Long, *J. Am. Chem. Soc.* **2011**, *133*, 5664.
[35] P. I. Ravikovitch, A. Vishnyakov, R. Russo, A. V. Neimark, *Langmuir* **2000**, *16*, 2311.
[36] J. Janek, W. G. Zeier, *Nat. Energy* **2023**, *8*, 230.
[37] H. Vogel, *Phys Z* **1921**, *22*, 645.
[38] G. S. Fulcher, *J Am Ceram Soc* **1925**, *8*, 339.
[39] G. Tammann, W. Hesse, *Z Anorg Allg Chem* **1926**, *156*, 245.
[40] K. Tan, S. Zuluaga, Q. Gong, P. Canepa, H. Wang, J. Li, Y. J. Chabal, T. Thonhauser, *Chem. Mater.* **2014**, *26*, 6886.
[41] P. Voepel, C. Seitz, J. M. Waack, S. Zahn, T. Leichtweiß, A. Zaichenko, D. Mollenhauer, H. Amenitsch, M. Voggenreiter, S. Polarz, B. M. Smarsly, *Cryst. Growth Des.* **2017**, *17*, 5586.
[42] H. Zhang, C. Li, M. Piszcz, E. Coya, T. Rojo, L. M. Rodriguez-Martinez, M. Armand, Z. Zhou, *Chem. Soc. Rev.* **2017**, *46*, 797.
[43] F. Zhu, H. Bao, X. Wu, Y. Tao, C. Qin, Z. Su, Z. Kang, *ACS Appl. Mater. Interfaces* **2019**, *11*, 43206.
[44] L. Du, B. Zhang, W. Deng, Y. Cheng, L. Xu, L. Mai, *Adv. Energy Mater.* **2022**, *12*, 1.
[45] P. G. Bruce, C. A. Vincent, *J. Electroanal. Chem.* **1987**, *225*, 1.
[46] W. Zhang, D. A. Weber, H. Weigand, T. Arlt, I. Manke, D. Schröder, R. Koerver, T. Leichtweiss, P. Hartmann, W. G. Zeier, J. Janek, *ACS Appl. Mater. Interfaces* **2017**, *9*, 17835.
[47] P. Pracht, F. Bohle, S. Grimme, *Phys. Chem. Chem. Phys.* **2020**, *22*, 7169.
[48] P. Pracht, S. Grimme, *Chem. Sci.* **2021**, *12*, 6551.
[49] S. Grimme, *J. Chem. Theory Comput.* **2019**, *15*, 2847.
[50] P. Pracht, E. Caldeweyher, S. Ehlert, S. Grimme, **2019**, https://doi.org/10.26434/chemrxiv.8326202.v1.
[51] C. Bannwarth, S. Ehlert, S. Grimme, *J. Chem. Theory Comput.* **2019**, *15*, 1652.
[52] S. Grimme, C. Bannwarth, P. Shushkov, *J. Chem. Theory Comput.* **2017**, *13*, 1989.
[53] S. Ehlert, M. Stahn, S. Spicher, S. Grimme, *J. Chem. Theory Comput.* **2021**, *17*, 4250.
[54] R. Ahlrichs, M. Bär, M. Häser, H. Horn, C. Kölmel, *Chem. Phys. Lett.* **1989**, *162*, 165.
[55] S. G. Balasubramani, G. P. Chen, S. Coriani, M. Diedenhofen, M. S. Frank, Y. J. Franzke, F. Furche, R. Grotjahn, M. E. Harding, C. Hättig, A. Hellweg, B. Helmich-Paris, C. Holzer, U. Huniar, M. Kaupp, A. Marefat Khah, S. Karbalaei Khani, T. Müller, F. Mack, B. D. Nguyen, S. M. Parker, E. Perlt, D. Rappoport, K. Reiter, S. Roy, M. Rückert, G. Schmitz, M. Sierka, E. Tapavicza, D. P. Tew, et al. *J. Chem. Phys.* **2020**, *152*, 184107.
[56] TURBOMOLE V7.5.1 a development of University of Karlsruhe and Forschungszentrum Karlsruhe GmbH, 1989–2007, TURBOMOLE GmbH, since 2007; available from https://www.turbomole.org (accessed: June 2021).
[57] K. Eichkorn, O. Treutler, H. Öhm, M. Häser, R. Ahlrichs, *Chem. Phys. Lett.* **1995**, *240*, 283.
[58] K. Eichkorn, O. Treutler, H. Öhm, M. Häser, R. Ahlrichs, *Chem. Phys. Lett.* **1995**, *242*, 652.
[59] K. Eichkorn, F. Weigend, O. Treutler, R. Ahlrichs, *Theor. Chem. Acc.* **1997**, *97*, 119.
[60] P. A. M. Dirac, R. H. Fowler, in *Proc. R. Soc. Lond. Ser. Contain. Pap. Math. Phys. Character* **1997**, Vol. *123*, pp. 714–733.
[61] J. C. Slater, *Phys. Rev.* **1951**, *81*, 385.
[62] J. P. Perdew, Y. Wang, *Phys. Rev. B* **1992**, *45*, 13244.
[63] J. P. Perdew, K. Burke, M. Ernzerhof, *Phys. Rev. Lett.* **1996**, *77*, 3865.
[64] J. P. Perdew, M. Ernzerhof, K. Burke, *J. Chem. Phys.* **1996**, *105*, 9982.
[65] S. Grimme, J. Antony, S. Ehrlich, H. Krieg, *J. Chem. Phys.* **2010**, *132*, 154104.
[66] S. Grimme, S. Ehrlich, L. Goerigk, *J. Comput. Chem.* **2011**, *32*, 1456.
[67] D. Aurbach, *Nonaqueous Electrochemistry*, CRC Press, Boca Raton **1999**.
[68] A. Schäfer, A. Klamt, D. Sattel, J. C. W. Lohrenz, F. Eckert, *Phys. Chem. Chem. Phys.* **2000**, *2*, 2187.
[69] A. Klamt, G. Schüürmann, *J. Chem. Soc. Perkin Trans.* **1993**, *2*, 799.
[70] R. S. Mulliken, *J. Chem. Phys.* **1955**, *23*, 1833.
[71] G. Kresse, J. Furthmüller, *Phys. Rev. B* **1996**, *54*, 11169.
[72] G. Kresse, J. Hafner, *Phys. Rev. B* **1993**, *47*, 558.
[73] G. Kresse, J. Hafner, *Phys. Rev. B* **1994**, *49*, 14251.
[74] G. Kresse, J. Furthmüller, *Comput. Mater. Sci.* **1996**, *6*, 15.